Kr environment in feldspathic glass and melt: A high pressure, high temperature X-ray absorption study

Céline Crépisson, Chrystèle Sanloup, Laurent Cormier, Marc Blanchard, Jessica Hudspeth, Angelika D Rosa, Olivier Mathon, Tetsuo Irifune

Kr environment in feldspathic glass and melt: a high pressure, high temperature X-ray absorption study

Céline Crépisson[a*], Chrystèle Sanloup[a], Laurent Cormier[b], Marc Blanchard[c], Jessica Hudspeth[a], Angelika D. Rosa[d], Olivier Mathon[d], Tetsuo Irifune[e]

[a]Sorbonne Université, CNRS, UMR 7193 - Institut des Sciences de la Terre de Paris (ISTeP), 4 place Jussieu, 75005, Paris, France

[b]Sorbonne Université, CNRS UMR 7590, MNHM, IRD, Institut de Minéralogie de Physique des Matériaux et de Cosmochimie (IMPMC), 75005 Paris, France

[c]Géosciences Environnement Toulouse (GET), Université de Toulouse, CNRS, IRD, UPS, 14 avenue Edouard Belin, 31400 Toulouse, France

[d]European Synchrotron Radiation Facility, ESRF, 71 Avenue des Martyrs, 38000 Grenoble, 6 France.

[e]Ehime University, Geodynamic Research Center, Matsuyama, Japan

[*]Corresponding author. Address : Céline Crépisson, Institut des Sciences de la Terre de Paris (ISTeP), Sorbonne Université, Case 110, 4 place Jussieu, 75005 Paris, France. Tel.: +33 1 44 27 60 64. Email : celine.crepisson@upmc.fr

Abstract

Noble gases are used to trace the evolution of the Earth's atmosphere and magmatic processes. However little is known about their solubility mechanisms in silicate melts or glasses, whereas it could be fundamental to interpret these data. We report here the first *in situ* X-ray absorption spectroscopy data at the Kr K-edge on a feldspathic Kr-bearing glass and melt (0.5 wt % Kr) up to 2.7 GPa and 1086°C. Kr fitting of the EXAFS signal shows that Kr is surrounded by oxygen atoms. Two Kr-O distances are identified: 2.49±0.1 Å and 3.32±0.1 Å. Results can be interpreted as two Kr populations. Kr surrounded by O atoms at 3.32±0.1 Å suggests a filling of the large cavities available in the silicate network, in agreement with previous studies. On the contrary, Kr surrounded by O atoms at 2.49±0.1 Å, and the observed + 0.6 eV shift of the edge position at high pressure, suggest Kr bonding to O atoms and Kr oxidation inside cages formed by the largest aluminosilicate rings (i.e. ~ 12-membered-rings). Present results show that heavy noble gases incorporation in silicate melts can no longer be considered as a passive filling of the voids.

Keywords

Krypton, XAS, silicate glass, silicate melt, high pressure

1. Introduction

Due to their supposed chemical inertia, high volatility, and high dilution, noble gases have been intensively studied by geochemists to understand the formation of the Earth's atmosphere, and to study mantle dynamics. None of Kr stable isotopes (^{78,80,82,83,84,86}Kr) is

purely radiogenic, and Pu and U fission yields are very low for Kr. Thus Kr cannot be used to constrain chronology of the atmosphere evolution, and as such has been less studied than He, Ne, Ar, and Xe. However, the small amount of radiogenic Kr makes it suitable to trace air component in fluid inclusions (Böhlke and Irwin, 1992). Earth atmospheric Kr isotope composition, unchanged since at least 3.3 Ga (Avice et al., 2017), falls in-between solar and chondritic compositions (Pepin, 1991). Kr isotopic ratios in CO_2 magmatic well gases that probed the continental lithosphere, showed a significant enrichment in ^{84}Kr and ^{86}Kr compared to the atmosphere (Holland et al., 2009). The discovery of Kr isotopic fractionation in these well gases, taken as a proxy of deep mantle gases, was interpreted as the signature of a primordial Kr chondritic component (Holland et al., 2009). Nevertheless Holland et al. (2009) argue that early degassing of an accreted primordial chondritic composition, followed by mass fractionation during atmosphere loss, fails to explain the composition of the modern atmosphere. Instead, late accretion of cometary material is assumed to explain Kr isotope signature of the atmosphere. Although very few samples have been analyzed for all Kr isotopes, mantle-derived basalts (MORBs, OIBs) have an atmospheric Kr isotopic composition (Moreira et al., 1998; Trieloff et al., 2000; Graham, 2002). This homogeneous composition could be due to atmospheric Kr recycling at subduction zones (Holland and Ballentine, 2006).

To explain highly precise Kr isotopic data, geochemists need an understanding of Kr behavior in silicate melts, including Kr solubility value and mechanism, as well as Kr degree of compatibility.

Fractionated fission Kr has also been observed in the Okhlo natural nuclear reactor. In nuclear plants, ^{85}Kr is a common fission product. Nuclear waste confinement by vitrification in SiO_2-rich glasses has been used for many years (Ojovan and Lee, 2011). Accumulation of Kr leads to the formation of nanobubbles where pressure may reach 2.6 GPa (Martin et al.,

2015) under high temperature generated by irradiation. Understanding of Kr behavior in silicate glasses is thus crucial for long nuclear waste storage.

The majority of studies dedicated to noble gases solubility in melts are based on analyses of recovered glassy samples, and did not directly investigate the noble gas structural environment in the silicate network, as noble gases can escape from the silicate structure at ambient conditions. These studies showed that noble gas solubility decreases with increasing radius (from He to Xe) (Caroll and Stolper, 1993, Lux, 1987, Shibata et al., 1998), and that this solubility strongly depends on the chemical composition of the melt. Noble gas solubility was first related to ionic porosity, i.e. the absolute volume of voids (Caroll and Stolper, 1993), whereas Shibata et al. (1998) showed that it was better inversely correlated to the number of non-bridging oxygen per silicon, even if the presence of Al may modify this trend (Bouhifd and Jephcoat, 2006). Based on these findings and noble gas relative chemical inertia, noble gases were supposed to passively fill the voids of the silicate network.

In situ structural data on the environment of heavy noble gases in silicate melts and glasses are scarce. Wulf et al. (1999) performed an X-ray absorption study at the Kr K-edge in a SiO_2 glass (1.97 wt % Kr). They identified a Kr-O distance of 3.45±0.1 Å, interpreted as corresponding to a local rearrangement of the silicate network into a local clathrasil-type environment around the Kr atom. The supposed chemical inertia of Kr and Xe, the most reactive of the noble gases, has been questioned throughout the past 15 years, with the synthesis of numerous Kr and Xe compounds (see Grochala, 2007 for a review). Bonding of Xe to O in compressed haplogranitic magmas had also been evidenced by *in situ* X-ray diffraction (Leroy et al. 2018).

In the present study, we perform *in situ* X-ray absorption spectroscopy (XAS) at the Kr K-edge, to specifically access Kr structural environment in a feldspathic (sanidine) glass.

Starting $(Na,K)AlSi_3O_8$ glass composition was chosen as representative of the chemistry of a major mineral of the continental crust, and proxy of silica-rich melts that can be generated at pressure reaching 2 GPa in orogenic contexts (Jimenez-Munt et al., 2008), and in subduction contexts from melting of hydrous basalt (Prouteau et al., 2001), or silica-rich sediments (Turner et al., 2012). Experiments were conducted at pressures (P) and temperatures (T) up to 2.7 GPa and 1086°C, relevant for both continental crust melting and subduction zone contexts.

2.Material and Methods

2.1 Sample: synthesis and characterization

The starting glass of Kr/Xe-bearing sanidine was synthesized in a piston cylinder press at 3.5 GPa and 1400°C for 24 hours before quenching. For this purpose, Xe and Kr were loaded as a 1:1 gaseous mix along with sanidine powder in a Pt capsule (Boettcher et al., 1989). Sanidine is a high-temperature feldspar, of atomic composition $(K_xNa_{1-x})AlSi_3O_8$ with x higher than 0.32 (Bendel and Schmidt, 2008). In our experiments, sanidine powder was obtained by grinding a natural sanidine mineral ($K_{0.52}Na_{0.43}Al_{1.05}Si_{2.96}O_8$, formula unit retrieved from electron microprobe analysis) from the Sorbonne Université mineralogical collection.

Starting glass and recovered sample were mounted in epoxy, polished and C-coated. They were observed by Scanning Electron Microscope (SEM) with a Zeiss Supra 55 (equipped with a field emission gun). Detection of Xe and Kr was optimized with an acceleration voltage of 20 keV and a working distance of 6.6 mm in backscatter mode.

Electron microprobe analyses (EMPA) were done on a CAMECA SX5, at CAMPARIS centre at Sorbonne Université. Operating conditions were 15 kV accelerating voltage, 10 nA beam current, and a focused beam for point analysis. We use the method from Montana et al. (1993) for Kr, which was calibrated by measuring the counts on neighboring elements (i.e. Rb). Xe was calibrated using a known standard analyzed by Particle-Induced X-ray Emission (data published in Leroy et al., 2018).

The synthesized starting glass is chemically homogeneous (based on SEM and EMP analyses) with presence of Kr/Xe gas bubbles indicating that saturation was reached. Contents of 2.2 wt % Xe (0.36 at %) and 0.5 wt % Kr (0.13 at %) were measured by electron microprobe analyses from an average of seven points of analysis in areas free of micrometric gas bubbles. Average composition in wt % of the starting glass is given in Table 1. Recovered sample was quenched from 1040°C and 2.7 GPa, where it reequilibrated as partial melt and feldspar crystals (Figure 1), following cooling from fully molten state (1415°C and 3 GPa) which was reached with the initial purpose to collect XAS data at the Xe-edge. Kr and Xe are only observed in the glass, with striking alignments of Kr/Xe gas nanobubbles (Figure 1). Average analyses of the recovered sample are given in Table 1, although degassing upon quenching prevents Xe and Kr contents to be determined by EMP analysis.

2.2 Experimental set-up

In-situ X-ray absorption spectroscopy (XAS) was performed on beamline BM23 at the ESRF, dedicated to general purpose XAS (Mathon et al., 2015). High pressure and temperature conditions up to 2.7 GPa and 1086°C (Table 2) were generated in a Paris Edinburgh Press (Besson et al., 1992). We used a cell assembly developed by Kono et al. (2014) and adapted from Yamada et al. (2011). More details on the cell-assembly and

experimental set-up can be found in Rosa et al. (2016). The sample (0.75 mm diameter and 1.5 mm height) was encapsulated in a synthetic nanopolycrystalline diamond (NPD) cylinder caped with Pt-Rh caps. The use of NPD prevents glitches from a single or polycrystalline diamond capsule, which deteriorate the XAS signal. Temperature was determined using calibration from Kono et al. (2014), and pressure using unit cell volume of hBN from the cell assembly (based on X-ray diffraction measurements) and equation of state from Le Godec et al. (2000). Error bars are ±50°C for temperature and ±0.2 GPa for pressure.

2.3 XRD and XAS measurements

Angle-resolved X-ray diffraction data were recorded on a MAR165 CCD at 15 keV. Image plates were integrated using Fit 2D software (Hammersley, 1997). Cell parameters of hBN were determined using POWDER CELL software (Kraus and Nolze, 1996).

XAS transmission measurements were performed first at the Kr K-edge (14326 eV) up to 2.7 GPa, upon increase of temperature up to 1086°C, and upon decrease of temperature down to 505°C, before quenching to room temperature (Table 2). Xe K-edge spectra were recorded following measurement at the Kr K-edge upon increasing temperature up to 1415°C and 3 GPa, and upon cooling to 1040°C at 2.7 GPa followed by quenching. Xe K-edge spectra are however not of sufficient quality to allow fitting, given the very small absorption jump (0.09 compared to 0.25 at the Kr K-edge), and are thus not shown here. Energy calibration of the edge position was made by frequent analyses of Kr gaseous standards. The beam size on the sample was 300 x 80 μm^2. Transmitted X-ray intensity was recorded by ionization chambers filled with gaseous Ar-He mixed gas. Signal was collected from 14244 eV to 14971 eV at the Kr K-edge (451 points analysis). Counting times, number of scans, and P/T conditions are

given in Table 2. Energy steps were adapted as a function of the edge position, each scan takes about 1 hour.

2.4 Processing of XAS data

The edge of the standard was fixed to 14326 eV, and the edge of each sample was recalibrated using the averaged edge value of two gaseous Kr standards taken before and after the sample measurement. For Kr standard, no significant shift of the Kr K-edge was noted (0.4 eV at the largest). After correction of edge position, data were cut at 14800 eV for better normalization.

Data processing was performed using ATHENA and ARTEMIS packages, based on the IFEFFIT programs (Ravel and Newville, 2005). Each scan was corrected with a pre-edge and a post-edge baseline. Position of the edge was determined by the position of the first derivative of the absorption. The intensity of the jump at the edge was then normalized to one. After merging of the scans collected at a given P/T condition, data were corrected using a background function. We used an automated background subtraction method (AUTOBKG) developed by Newville (Newville, 2001) and implemented in the ATHENA software. This correction minimizes the features below the first atom-atom distance in the R-space. R_{bkg} was fixed to 1.2 Å.

To fit the data at the Kr K-edge, we used a k-range of ~ 2.2-6.5 $Å^{-1}$ (Table 3), due to low signal to noise ratio at higher k values. A small k-range ensures that all the different contributions to the Fourier transform are not artifacts but really arise from neighboring atoms. Real part of backward Fourier transform was exported to ARTEMIS software to be fitted using R-range ~ 1.1-3.8 Å (Table 3). Fitting made on real part of backward Fourier transform ensures that all XANES and noise contributions are removed from the EXAFS

signal. Fit parameters include: amplitude reduction factor (S0), average distances of the neighboring atom to the central Kr atom, Debye Waller factor (σ^2), and difference of edge position compared to standard value (ΔE_0). ΔE_0 values remain smaller than 7 eV, attesting consistency of the fits. It was necessary to add a third order anharmonic cumulant expansion fitting parameter (C3) for high pressure or high temperature measurements (Stern et al, 1991; Farges et al., 1994). C3 is a measure of the asymmetry of the signal disorder, which arises in glasses from configurational disorder associated to thermal vibration at high pressure and/or high temperature conditions. The absolute value of C3 remains smaller than 0.009 $Å^3$, similar to values found by Cochain et al. (2015) on silicate glasses and melts at high pressure and temperature conditions. As no Kr standard was analyzed in the course of the experiment besides Kr gas, it is not possible to determine coordination numbers (CN). We therefore fixed S0 at a common value of 0.79, and fixed the value of CN. In total, seven parameters must be fitted (first interatomic distance, σ^2 and C3 for the two contributions and ΔE_0) whereas N, the number of variables to fit, cannot exceed (Teo, 1986):

$$N = \frac{2\Delta R \Delta k}{\pi} \qquad (1)$$

In our case $\Delta k \approx 4.3$ $Å^{-1}$ and $\Delta R \approx 2.8$ Å. Therefore maximum number of parameters N, which can be fitted is ~ 7.7, indicating that we can theoretically fit our data as exposed above.

3.Results and Discussion

3.1. XAS data at the Kr K-edge

XAS data were recorded at ambient conditions, at high pressure and high temperature, and after quenching (Table 2). Potassic sanidine ($KAlSi_3O_8$) is expected to melt around 1500°C at 2.6-2.7 GPa (Boettcher et al., 1984). Reports on the $KAlSi_3O_8$-$NaAlSi_3O_8$ join under anhydrous conditions at 1 atm showed that melting temperature of $KAlSi_3O_8$ drops by 100°C for our starting composition ($Na_{0.43}K_{0.52}Al_{1.05}Si_{2.96}O_8$, atomic formula retrieved from EMPA) (Schairer, 1950). Glass transition temperature (Tg) of felspathic glass at 1 atm was found in-between 907-948°C based on viscosity measurements (Petermann et al., 2008; Richet and Bottinga, 1984). Moreover, viscosity is shown to decrease from 0 GPa to 2.5 GPa for both sanidine melt (White and Montana, 1990) and albite melt (Kushiro, 1978). Thus Tg is expected to be even lower than 907-948°C at our pressure conditions. Therefore our measurements at 1086°C (and potentially at 920°C) were recorded above Tg and before recrystallization, i.e. on the supercooled liquid, behaving like a melt. Well-defined oscillations are visible in the X-ray absorption signal, and clearly differ from the signature of Kr gas and Kr liquid under pressure (Di Cicco et al., 1996) (Figures 2 and 3).

Rapid damping of the EXAFS signal indicates disorder beyond the first shell. We compare in Figure 3 our data with the k^2-weighted EXAFS function recorded at 27°C on UO_2 (8 at % Kr) previously implanted with Kr ions (Martin et al., 2015). Oscillations observed after 4 $Å^{-1}$ clearly differ from our data sets. The magnitude of the Fourier transform (k-range used is displayed in Table 3) clearly shows two peaks at all measurement conditions (Figure 4), indicating that two distances contribute to the signal, with the main distance at ~ 1.9 Å, while Martin et al. (2015) reports a main distance at 3.44 Å. Kr environment in sanidine glass is therefore different from that observed by Martin et al. (2015) in UO_2, i.e. Kr nanoclusters. There is no noticeable change in the room temperature glass with pressure: data at ambient pressure and after quenching at 1.4 GPa being similar (Figures 2, 3 and 4). The relative intensity of the two peaks however varies with temperature, the magnitude of the Fourier

transform (Figure 4) being different at ambient temperature, at 505°C and 706°C, and especially in the melt at 920°C and 1086°C.

3.2 Resolving Kr environment in sanidine glass and melt

Variations of fitted Kr-O distances over our experimental P/T range are within error (i.e. ±0.1 Å). We thus evaluate averaged Kr-O distances for the whole P/T range, two Kr-O distances are identified at 2.49±0.1 Å and 3.32±0.1 Å (Table 3, Fig. 5). No other neighboring atom than oxygen could fit the observed XAS signal, although we considered other atomic pairs such as Kr-Kr, Kr-Si, Kr-Na, or Kr-K. Identified distances confirm the absence of Kr neighbors. Indeed Kr-Kr distance in solid cubic Kr is 3.68 Å at 2 GPa and room temperature (Di Cicco et al., 1996). We can interpret these results as two distinct populations of Kr located in two different sites of the silicate network. Results clearly differ from Wulf et al. (1999), who only reported a Kr-O distance at 3.45 Å, as shown in Figure 5.

At ambient condition, there is no non-bridging oxygen in sanidine glass ($KAlSi_3O_8$), and Al coordination number is four for all Al atoms (Thompson et al., 2011). Study of an albite glass ($NaAlSi_3O_8$) quenched from the melt at 2.6 GPa showed that less than 3% of Al atoms present a coordination number of five, whereas all remaining Al atoms have a coordination number of 4 (Gaudio et al., 2015). Sanidine glass is thus fully polymerized, with all Na^+/K^+ compensating the charge deficit created by the presence of Al^{3+} in tetrahedral position. Molecular dynamic simulations showed that in soda aluminosilicate glass, for Na/Si=1, distribution of the aluminosilicate rings at ambient pressure varies from 2 to 13 membered-rings, with 6 or 7 membered-rings being the most present ring population (Xiang et al., 2013). Similarly, at ambient pressure, a ring size distribution from 2 to 12-membered rings is predicted for silica glass with 6 to 7 membered-rings being the dominant ring population (Kohara et al. 2011; Guerette et al., 2015). To our knowledge, no pore size

distribution data is available for our glass composition. Based on the similarity of ring size distribution between aluminosilicate and silica glass, we assume that size of cages within aluminosilicate rings range from 0.9 Å to 5.9 Å in diameter, like in silica glass (Guerette et al., 2015). This size distribution indicates the presence of 5-5.9 Å-diameter voids, inside the largest (i.e. ~ 12-membered) aluminosilicate rings. The Kr-O distance of 2.49±0.1 Å is therefore compatible with a Kr atom located inside the largest observed rings of the silicate network. This Kr-O distance falls in-between the sum of covalent radii of Kr and O (1.16 Å and 0.66 Å respectively (Cordero et al., 2008)) and the sum of ionic radii of Kr^{0} and O^{2-} (respectively 1.78 Å for a coordination number of 6 (Zhang et al. 1995) and 1.4 Å (Shannon, 1976)). This result indicates that Kr is interacting closely with the neighboring oxygen atoms, suggesting an oxidation of Kr. Under pressure, the edge position shifts by + 0.6 eV (Figure 6). Shift of the edge can be related to change in the oxidation state as observed for Cu, Co, Fe, Mn (e.g. Klysubun et al., 2015). This observation further supports a change in Kr oxidation due to Kr-O bonding. Kr is in the oxidation state II in most of Kr compounds synthesized, such as KrF_2, KrF^+ or $Kr_2F_3^+$ (Grosse et al., 1963, Burbank et al., 1972, Lehmann et al., 2001). Kr oxidation number is expected to increase compared to gaseous Kr, if Kr is surrounded by several O atoms.

The Kr-O distance of 3.32±0.1 Å cannot correspond to the presence of Kr atoms inside aluminosilicate rings, as the size distribution is limited to 5.9 Å in diameter. This larger Kr-O distance is similar to the 3.45±0.1 Å distance reported in SiO_2 glass at ambient pressure and 5 K (Wulf et al., 1999), and close to predictions from first principle molecular dynamics. Zhang et al. (2009) indeed found Kr-O = 3.5 Å in liquid silica, with Kr coordination number varying from 10 to 15 depending on pressure. Similar result was found by Guillot and Sator (2012) using molecular dynamics with Kr-O = 3.45 Å in silica melt and 3.31 Å in rhyolite melt. This large distance can be explained by the formation of large cavities in the melt where noble

gases are accommodated, in agreement with a passive filling of the void space, or with a clathrasil-like environment (Wulf et al., 1999). Contribution of Kr fluid to this longer distance cannot be ruled out if the few Kr bubbles observed on starting and quenched samples are not fully homogenized with the melt at high pressure and temperature.

Disappearance of the larger Kr-O distance at higher temperatures (Figure 4), indicates that smaller Kr-O distance is more favorable, possibly with the increase of Kr reactivity. Moreover, the Debye Waller factor associated with the smallest Kr-O distance ($\sigma^2 1$), is twice larger at room temperature than at high temperature (Table 3), suggesting that ordering of the smaller Kr-O environment is higher. Measurements at high pressures and temperatures are all above Kr melting point, whereas measurement after quenching at 1.4 GPa is below Kr melting point (Ferreira and Lobo, 2008). Kr reactivity therefore seems enhanced above Kr melting curve, suggesting that it is pressure-induced, i.e. it favors smaller volume, as observed for Xe incorporation in olivine (Sanloup et al., 2011). Besides, the larger Kr-O distance vanishes in the melt, i.e. at 920°C and 1086°C (Figure 4), indicating structural changes between the melt and the glass. A complementary explanation could be a contribution of Kr fluid to the longer Kr-O distance, which would diminish with temperature due to the increase of Kr solubility in the melt.

Current knowledge of glass and silicate melt structures therefore supports the hypothesis of two Kr populations, with one population of Kr, oxidized and possibly located in the largest aluminosilicate rings, and one population filling the large cavities available in the silicate network.

4.Conclusion

The present work provides evidence for the reactivity of Kr with silicate that adds up to the previously reported evidences of Kr reactivity (Grochala, 2007). Kr oxidizes in feldspathic glass and melt at high P/T conditions as shown by creation of short Kr-O bonds (2.49±0.1 Å) and shift of the edge position. Kr behavior in compressed magmas thus appears to be intermediate between that of an inert noble gas (He, Ne, Ar) and that of the heavier Xe. Indeed Xe is shown to fully oxidize in compressed haplogranitic melts with Xe in the most abundant 6-membered rings containing 12 nearest O, Xe-O distance of 2.05±0.05 Å is similar to distance reported for covalent Xe-O bond in crystalline silicates (Probert, 2010; Kalinowski et al., 2014; Crépisson et al., 2018). Both results question the supposed passive filling of the void spaces by heavy noble gases (Caroll and Stolper, 1993; Shibata et al., 1998), and the assumption that all noble gases can be considered as zero-charge cation (e.g. Brooker et al., 2003).

Creation of short Kr-O bonds in sanidine melt at depth, supports the role of Kr recycling at subduction zones, proposed by Holland and Ballentine (2006), as Kr will efficiently dissolve in the melt. Hydrated melts will now need to be studied to test the influence of water, which is thought to dramatically increase noble gases solubility (Nuccio and Paonita, 2000).

The Earth's atmosphere is depleted in heavy Kr isotopes compared to chondrites (Holland et al., 2009). Observation of short Kr-O bonds in silicate melt, implying Kr reactivity, suggests potential isotopic fractionation during partial-melting and melt percolation, as shown for instance for Cu (Huang et al., 2017), and / or during fluid / melt interactions either upon fluid injection at depth in subduction zones or degassing during magma ascent. This phenomenon could have contributed to enrichment of well gases from the continental lithosphere in heavy Kr isotopes, while most of the samples from the Earth's mantle (OIBs and MORBs) have an atmospheric Kr isotopic composition due to intense recycling.

Acknowledgements:

We thank Omar Boudouma for SEM analyses, the Sorbonne Université Mineralogical collection for providing the natural sanidine sample, and the European Synchrotron Radiation Facilities for allocating beamtime to this work. This work was supported by the European Community's Seventh Framework Programme (FP7/2007-2013), European Research Council starting grant to C. Sanloup [grant numbers 312284 and 259649].

372 **References:**

373 Avice G., Marty B., and Burgess R. 2017. The origin and degassing history of the Earth's
374 atmosphere revealed by Archean xenon. Nature communications, 8, 15455.

375 Bendel V. and Schmidt B.C. 2008. Raman spectroscopic characterisation of disordered alkali
376 feldspars along the join $KAlSi_3O_8$–$NaAlSi_3O_8$: application to natural sanidine and
377 anorthoclase. European Journal of Mineralogy, 20, 1055–1065.

378 Besson J.M., Hamel G., Grima T., Nelmes R.J., Loveday J.S., Hull S., and Häusermann D.
379 1992. A large volume pressure cell for high temperature. High Pressure Research, 8, 625-630.

380 Boettcher A., Guo Q., Bohlen S., and Hanson B. 1984. Melting in feldspars-bearing systems
381 to high pressures and the structures of aluminosilicate liquids. Geology, 12, 202-204.

382 Boettcher S.L., Guo Q., and Montana A. 1989. A simple device for loading gases in high-
383 pressure experiments. American Mineralogist, 74, 1383-1384.

384 Böhlke J.K. and Irwin J.J. 1992. Brine history indicated by argon, krypton, chlorine, bromine,
385 and iodine analyses of fluid inclusions from the Mississippi Valley type lead-fluorite-barite
386 deposits at Hansonburg, New Mexico. Earth and Planetary Science Letters, 110, 51-66.

387 Bouhifd A. and Jephcoat A.P. 2006. Aluminium control of Argon solubility in silicate melts
388 under pressure. Nature, 439, 961-964.

389 Brooker R.A., Du Z., Blundy J.D., Kelley S.P., Allan N.L., Wood B.J., Chamorro E.M.,
390 Wartho J.A., Purton J.A. 2003. The 'zero charge' partitioning behaviour of noble gases during
391 mantle melting. Nature. 423, 6941, 738-741.

392 Burbank R.D., Falconer W.E., and Sunder W.A. 1972. Crystal Structure of Krypton
393 Difluoride at -80°C. Science, 178, 1285-1286.

Carroll M.R. and Stolper E.M. 1993. Noble gas solubilities in silicate melts and glasses: New experimental results for argon and the relationship between solubility and ionic porosity. Geochimica et Cosmochimica Acta, 57, 5039-5051.

Cochain B., Sanloup C., De Grouchy C., Crépisson C., Bureau H., Leroy C., Kantor I., and Irifune T. 2015. Bromine speciation in hydrous silicate melts at high pressure. Chemical Geology, 404, 18-26.

Cordero B., Gomez V., Cremades E., Alvarez S. 2008. Covalent radii revisited. Dalton Transactions, 2832-2838.

Crépisson C., Blanchard M., Balan E., and Sanloup C. 2017. New constraints on Xe incorporation mechanisms in olivine from First-principles calculation, Geochimica et Cosmochimica Acta.

Di Cicco A., Filipponi A., Itié J-P., and Polian A. 1996. High-pressure EXAFS measurements of solid and liquid Kr. Physical Review B, 54, 9086-9098.

Farges F., Brown G.E., Calas G., Galoisy L., and Waychuna G.A. 1994. Structural transformation in Ni-bearing $Na_2Si_2O_5$ glass and melt. Geophysical Research Letters, 21, 1931-1934.

Ferreira A.G.M., and Lobo L.Q. 2008. The fusion curves of xenon, krypton, and argon. The Journal of Chemical Thermodynamics, 40, 618–624.

Gaudio S.J., Lesher C.E., Maekawa H., and Sen S. 2015. Linking high-pressure structure and density of albite liquid near the glass transition. Geochimica et Cosmochimica Acta, 157, 28–38.

Graham D.W. 2002. Noble gas isotope geochemistry of Mid-Ocean Ridge Basalt and Ocean Island Basalts: characterization of mantle source reservoirs. in *Noble gases in Geochemistry and Cosmochemistry*, Reviews in Mineralogy and Geochemistry, 247-318.

418 Grochala W. 2007. Atypical compounds of gases, which have been called ‘noble’. Chemical
419 Society Reviews, 36, 1632-1655.

420 Grosse, A.V., Kirshenbaum, A.D., Streng, A.G, and Streng L.V. 1963. Krypton Tetrafluoride:
421 Preparation and Some Properties. Science, 139, 1047-1048.

422 Guerette M., Ackerson M.R., Thomas J., Yuan F., Watson E.B., Walker D., and Huang L.
423 2015. Structure and Properties of Silica Glass Densified in Cold Compression and Hot
424 Compression. Nature Scientific Reports, 5.

425 Guillot B., and Sator N. 2012. Noble gases in high-pressure silicate liquids: A computer
426 simulation study. Geochimica et Cosmochimica Acta, 80, 51-69.

427 Hammersley A. 1997. FIT2D: An Introduction and Overview. Technical Report
428 No.ESRF97HA02, ESRF.

429 Holland G., and Ballentine C. 2006. Seawater subduction controls the heavy noble gas
430 composition of the mantle. Nature, 441, 186-191.

431 Holland G., Cassidy M., and Ballentine C.J.. 2009. Meteorite Kr in Earth’s Mantle Suggests a
432 Late Accretionary Source for the Atmosphere. Science, 326, 1522-1525.

433 Huang J., Huang F., Wang Z., Zhang X., Yu H. 2017. Copper isotope fractionation during
434 partial melting and melt percolation in the upper mantle: Evidence from massif peridotites in
435 Ivrea-Verbano Zone, Italian Alps. Geochimica et Cosmochimica Acta, 211, 48-63.

436 Jiménez-Munt I., Fernandez M., Vergés J., and Platt J.P. 2008. Lithosphere structure
437 underneath the Tibetan Plateau inferred from elevation, gravity, and geoid anomalies. Earth
438 and Planetary Science Letters, 267, 276-289.

439 Kalinowski J., Rasanen M., Gerber R.B. 2014. Chemically-bound xenon in fibrous silica.
440 Physical Chemistry Chemical Physics, 16, 11658–11661.

441 Klysubun W., Hauzenberger C.A., Ravel B., Klysubun P., Huang Y., Wongtepa W.,and
442 Sombunchoo P. 2014. Understanding the blue color in antique mosaic mirrored glass from the
443 Temple of the Emerald Buddha, Thailand. X-ray spectrometry, 44, 116-123.

444 Kohara S., Akola J., Morita H. , Suzuya K., Weber J.K.R., Wilding M.C., and Benmore C.J.
445 2011. Relationship between topological order and glass forming ability in densely packed
446 enstatite and forsterite composition glasses. PNAS, 108, 14780-14785.

447 Kono Y., Park C., Kenney-Benson C., Shen G., and Wang Y. 2014. Toward comprehensive
448 studies of liquids at high pressures and high temperatures: Combined structure, elastic wave
449 velocity, and viscosity measurements in the Paris–Edinburgh cell. Physics of the Earth and
450 Planetary Interiors, 228, 269-280.

451 Kraus W. and Nolze G. 1996. POWDER CELL - a program for the representation and
452 manipulation of crystal structures and calculation of the resulting X-ray powder patterns.
453 Journal of Applied Crystallography, 29, 301-303.

454 Kushiro I. 1978. Viscosity and structural changes of albite ($NaAlSi_3O_8$) melt at high
455 pressures. Earth and Planetary Science Letters, 41, 87-90.

456 Le Godec Y., Solozhenko V.L., Mezouar M., Besson J-M., and Syfosse G. 2000. In situ X-ray
457 diffraction studies of formation of cubic and hexagonal graphite-like boron nitride by the
458 reaction of elemental boron with supercritical hydrazine. Science and Technology of High
459 Pressure. Universities Press, Hyderabad, India, 2, 1031-1034.

460 Lehmann J.F., Dixon D.A., and Schrobilgen G. 2001. X-ray Crystal Structures of alpha-KrF2,
461 [KrF][MF6] (M=As, Sb, Bi), Kr2F3][SbF6].KrF2, [Kr2F3]2[SbF6]2.KrF2, and
462 Kr2F3][AsF6] .[KrF][AsF6]; Synthesis and Characterization of [Kr2F3][PF6].nKrF2; and
463 Theoretical Studies of KrF2, KrF+, Kr2F3+, and the [KrF][MF6](M = P, As, Sb, Bi) Ion
464 Pairs. Inorganic Chemistry, 40, 3002-3017.

Leroy C. Sanloup C., Bureau H., Schmidt B.C., Konopkova Z., Raepsaet C. 2018. Bonding of xenon to oxygen in magmas at depth. Earth and Planetary Science Letters, accepted.

Lux G. 1987. The behavior of noble gases in silicate liquids: Solution, diffusion, bubbles and surface effects, with applications to natural samples. Geochimica et Cosmochimica Acta, 31, 1549-1560.

Martin P.M., Vathonne E., Carlot G., Delorme R., Sabathier C., Freyss M., Garcia P., Bertolus M., Glatzel P., and Proux O. 2015. Behavior of fission gases in nuclear fuel: XAS characterization of Kr in UO_2. Journal of Nuclear Materials, 466, 379-392.

Mathon O., Beteva A., Borrel J., Bugnazet D., Gatla S., Hino R., Kantor I., Mairs T., Munoz M., Pasternak S., Perrina F., and Pascarelli S. 2015. The time-resolved and extreme conditions XAS (TEXAS) facility at the European Synchrotron Radiation Facility: the general-purpose EXAFS bending-magnet beamline BM23. Journal of synchrotron radiation, 22, 1548-1554.

Meshik A.P., Kehm K., Hohenberg C.M. 2000. Anomalous xenon in zone 13 Okelobondo. Geochimica et Cosmochimica Acta, 64, 9, 1651-1661.

Montana A., Guo Q., Boettcher S., White B.S., and Brearley M. 1993. Xe and Ar in high-pressure silicate liquids. American Mineralogist, 78, 1135-1142.

Moreira M., Kunz J., and Allègre J.C. 1998. Rare gas systematics in popping rock: Isotopic and elemental compositions in the upper mantle. Science, 279, 1178-1181.

Newville M. 2001. EXAFS analysis using FEFF and FEFFIT. Journal of Synchrotron Radiation, 8, 96-100.

Nuccio P.M., and Paonita A. 2000. Investigation of the noble gas solubility in H2O-CO2 bearing silicate liquids at moderate pressure II: the extended ionic porosity (EIP) model. Earth and Planetary Science Letters, 183, 499-512.

Ojovan M.I., and Lee W. E. 2010. Glassy wasteforms for nuclear waste immobilization. Metallurgical and Materials Transactions A, 42, 4, 837-851.

Pepin R. 1991. On the origin and early evolution of terrestrial planet atmospheres and meteoritic volatiles. Icarus, 92, 2–79.

Pertermann, M., Whittington, A.G., Hofmeister, A.M., Spera F.J., Zayak J. 2008. Transport properties of low-sanidine single-crystals, glasses and melts at high temperature. Contributions to Mineralogy and Petrology, 155, 689-702.

Probert, M.I.J. 2010. An ab initio study of xenon retention in α-quartz. Journal of Physics of Condensed Matter, 22, 025501.

Prouteau, G., Scaillet, B., Pichavant, M., and Maury, R. 2001. Evidence for mantle metasomatism by hydrous silicic melts derived from subducted oceanic crust. Nature, 410, 6825, 197–200.

Ravel B., and Newville M. 2005. ATHENA, ARTEMIS, HEPHAESTUS: data analysis for X-ray absorption spectroscopy using IFEFFIT. Journal of Synchrotron Radiation, 12, 537–541.

Richet P, and Bottinga Y. 1984. Glass transitions and thermodynamic properties of amorphous SiO_2, $NaAlSi_nO_{2n+2}$ and $KAlSi_3O_8$. Geochimica et Cosmochimica Acta, 48, 3, 453-470.

Rosa A.D., Pohlenz J., de Grouchy C., Cochain B., Kono Y., Pasternak S., Mathon O., Irifune T., and Wilke M. 2016. *In-situ* characterization of liquid network structures at high pressure and temperature using X-ray Absorption Spectroscopy coupled with the Paris-Edinburgh press. High Pressure Research, 36, 332-347.

Sanloup C., Schmidt B.C., Gudfinnsson G., Dewaele A., and Mezouar M. 2011. Xenon and Argon: a contrasting behavior in olivine at depth. Geochimica et Cosmochimica Acta, 75, 6271–6284.

Schairer J. F. 1950. The alkali-feldspar join in the system $NaAlSiO_4$-$KAlSiO_4$-SiO_2. The

514 Journal of Geology, 58, 512-517.

515 Shannon R.D. 1976. Revised effective ionic radii and systematic studies of interatomic
516 distances in halides and chalcogenides. Acta Crystallographica, A32, 751-767.

517 Shibata T., Takahashi E., and Matsuda J.I. 1998. Solubility of neon, argon, krypton, and
518 xenon in binary and ternary silicate systems: A new view on noble gas solubility. Geochimica
519 et Cosmochimica Acta, 62, 1241-1253.

520 Stern E.A., Livins P., and Zhang Z. 1991. Thermal vibration and melting from a local
521 perspective. Physical review B, 43, 8850-8860.

522 Thompson L.M. and Stebbins J.F. 2011. Non-bridging oxygen and high-coordinated
523 aluminum in metaluminous and peraluminous calcium and potassium aluminosilicate glasses:
524 High-resolution ^{17}O and ^{27}Al MAS NMR results. American Mineralogist, 96, 841–853.

525 Trieloff M., Kunz J., Clague D., Harrison D., and Allègre J.C. 2000. The nature of pristine
526 noble gases in mantle plumes. Science, 288, 5468, 1036-1038.

527 Turner, S., Caulfield, J., Turner, M., vanKeken, P., Maury, R., Sandiford, M., and Prouteau,
528 G. 2012. Recent contribution of sediments and fluids to the mantle's volatile budget. Nature
529 Geoscience, 5, 1, 50–54.

530 White B.S., and Montana A. 1990. The effect of H_2O and CO_2 on the viscosity of sanidine
531 liquid at high pressures. Journal of Geophysical Research: Solid Earth Banner, 95 (B10),
532 15683-15693

533 Wulf R., Calas G., Ramos A., Büttner H., Roselib K., and Rosenhauer M. 1999. Structural
534 environment of krypton dissolved in vitreous silica. American Mineralogist, 84, 1461–1463.

535 Xiang Y., Du J., Smedskjaer M.M., and Mauro J.C. 2013. Structure and properties of sodium
536 aluminosilicate glasses from molecular dynamics simulations. The Journal of Chemical
537 Physics, 139.

Yamada A., Wang Y., Inoue T., Yang W., Park C., Yu T., and Shen G. 2011. High-pressure x-ray diffraction studies on the structure of liquid silicate using a Paris–Edinburgh type large volume press. Review of Scientific Instruments, 82.

Zhang Y. and Xu Z.. 1995. Atomic radii of noble gas elements in condensed phases. American Mineralogist, 80, 670-675.

Zhang L., Van Orman J.A., and Lacks D.J. 2009. Effective radii of noble gas atoms in silicate from first principles molecular simulation. American Mineralogist, 94, 600-609.

Table 1: Average composition of the starting glass (7 data points) and recovered sample (20 data points both in the glassy and crystalline parts) in oxide wt %, in brackets: standard deviation.

	Na_2O	**SiO_2**	**Al_2O_3**	**K_2O**	**CaO**	**Xe**	**Kr**	**Total**
Starting material	4.80 (0.2)	63.6 (0.40)	19.2 (0.14)	8.70 (0.24)	0.78 (0.05)	2.18 (0.04)	0.52 (0.05)	99.7 (0.47)
Recovered sample	2.9 (0.6)	65 (1)	19.8 (0.6)	11(1)	0.3 (0.2)	[0-1.3]*	[0-0.5]*	100(1)

** due to degassing upon quenching Kr and Xe contents cannot be properly evaluated by EMPA. Ranges of analyzed contents are given as an indication.*

Table 2: P/T conditions and state of the sample for each XAS measurement. n.s = number of scans, count. time = counting time per point analysis (451 point analysis).

Kr K-edge				
P (GPa)	**T (°C)**	**state**	**n.s**	**count. time**
0	20	glass	7	2s
2.6	920	melt	4	2s
2.7	1086	melt	5	2s
2	706	glass	5	2s
2	505	glass	5	2s
1.4	20	quench	4	2s

Table 3: Pressure-Temperature conditions and EXAFS-derived structural parameters. Conservative error bars are ± 0.05 eV for ΔE_0, ± 0.1 Å for Kr-O distances and ± 0.05 Å² for σ^2.

P (GPa)	T (°C)	k-range (Å^{-1})	R-range (Å)	ΔE_0 (eV)
0	20	2.2 - 6.5	1.1 - 3.5	3.32
2.6	920	2.3 - 6.5	1.2 - 4.0	6.09
2.7	1086	2.3 - 6.5	1.1 - 3.8	7.00
2	706	2.3 - 6.5	1.1 - 3.5	6.45
2	505	2.3 - 6.5	1.1 - 3.8	5.84
1.4	20	2.2 - 6.5	1.1 - 4.0	3.50
P (GPa)	**T (°C)**	**Kr-O1 (Å)**	**$\sigma^2$1 (Å^2)**	**C3$_1$ (Å^3)**
0	20	2.42	0.025	-
2.6	920	2.45	0.009	0.0021
2.7	1086	2.51	0.014	0.0078
2	706	2.53	0.009	0.0085
2	505	2.53	0.012	0.0076
1.4	20	2.49	0.021	0.0035
P (GPa)	**T (°C)**	**Kr-O2 (Å)**	**$\sigma^2$2 (Å^2)**	**C3$_2$ (Å^3)**
0	20	3.38	0.048	-
2.6	920	3.27	0.040	-0.0090
2.7	1086	3.37	0.042	0.0090

	2	706	3.34	0.064	-0.0034
	2	505	3.29	0.045	-0.0090
	1.4	20	3.30	0.049	-0.0057

Figure 1: SEM images in backscatter mode of recovered sample after XAS measurements. Feldspars recrystallized upon cooling to 1040°C at 2.7 GPa, coexisting with partial melt recovered as a glass upon quenching. Kr/Xe-nanobubbles (bright dots) are visible.

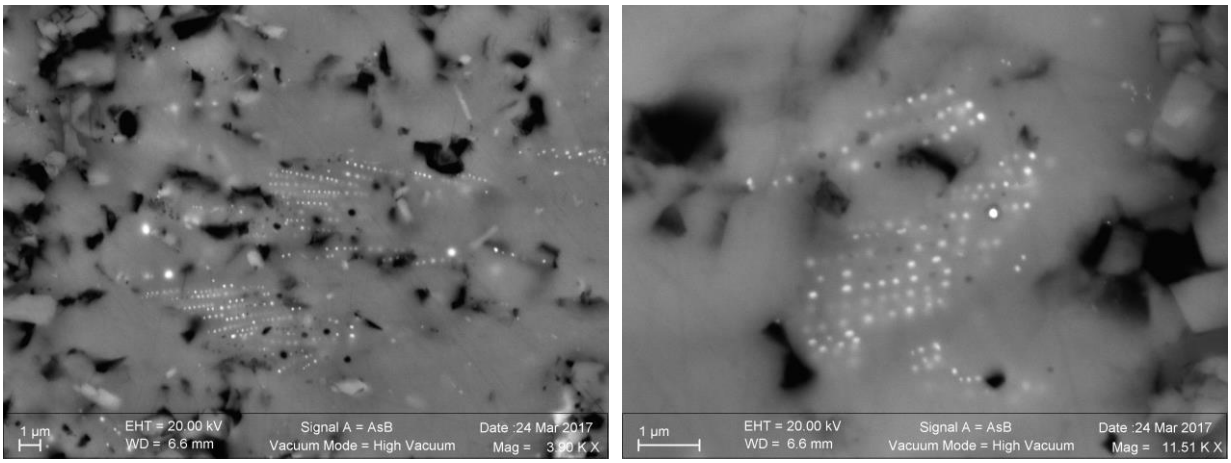

Figure 2: Normalized X-ray absorption spectra for sanidine glass and supercooled liquid, gaseous Kr at ambient conditions, and liquid Kr at 0.75 GPa (Di Cicco et al., 1996).

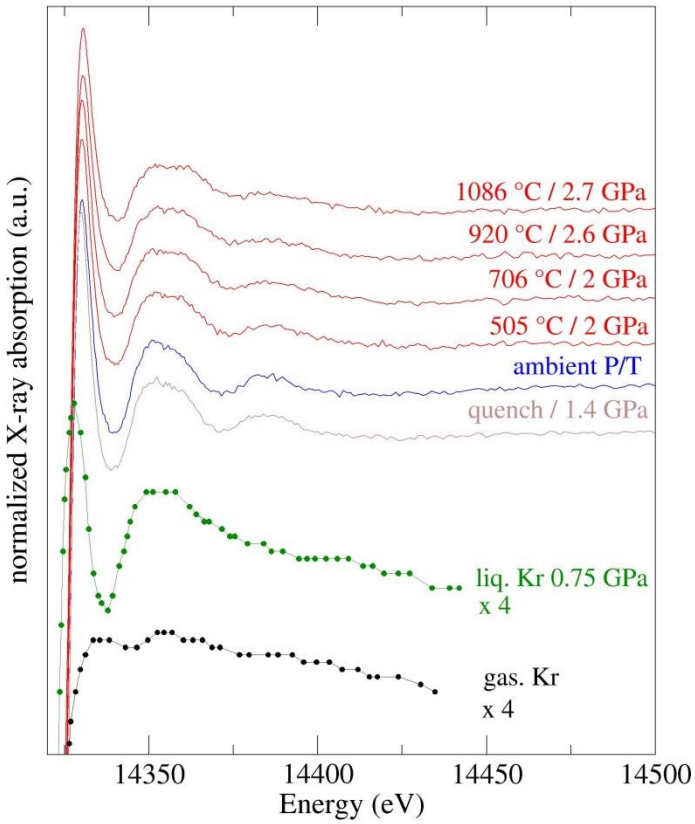

Figure 3: k^2-weighted EXAFS function for sanidine glass and supercooled liquid (color coding: same as Figure 2), and for UO_2 at room conditions (Martin et al., 2015).

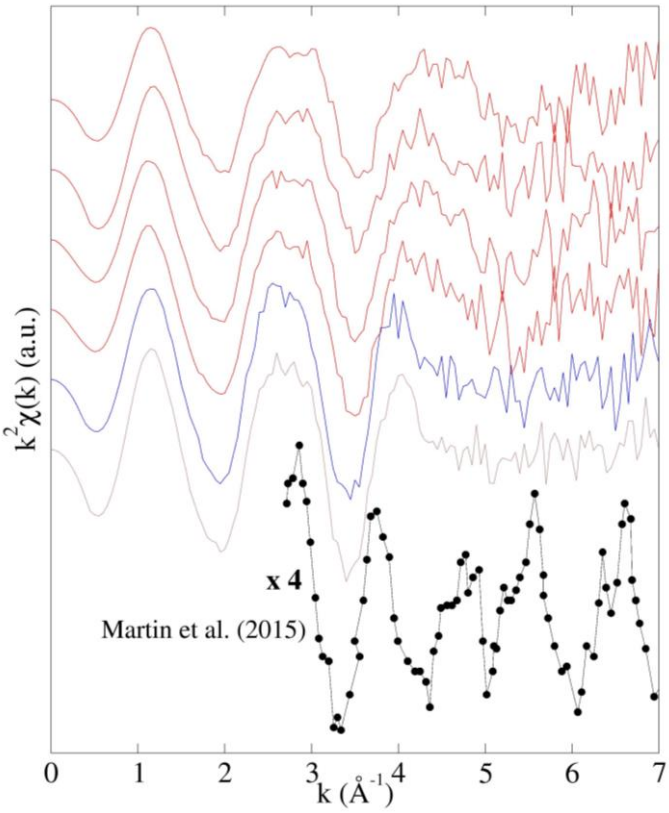

Figure 4: Magnitude of the Fourier transform of the k^2-weighted Kr EXAFS function without phase correction (same samples as Figure 3). The peak observed at ~1.9 Å corresponds to Kr-O = 2.49 Å, and the peak at ~2.9 Å corresponds to Kr-O = 3.32 Å. A general decrease of the amplitude is observed with increasing temperature (as noticed by Stern et al., 1991).

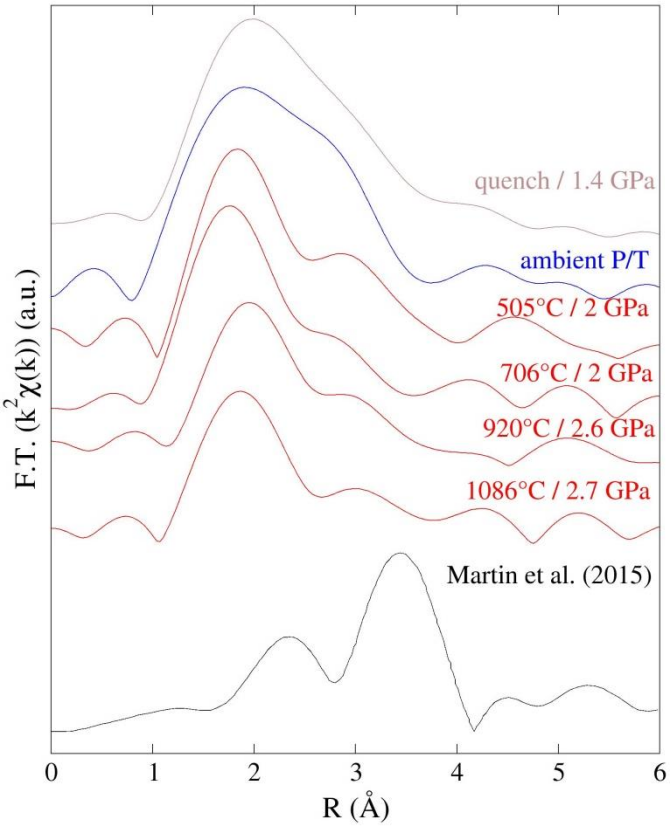

Figure 5: Real-part of backward Fourier transform (in dashed lines) and fit to the data (plain black line) for sanidine glass and supercooled liquid, and Kr-bearing SiO_2 glass (Wulf et al., 1999).

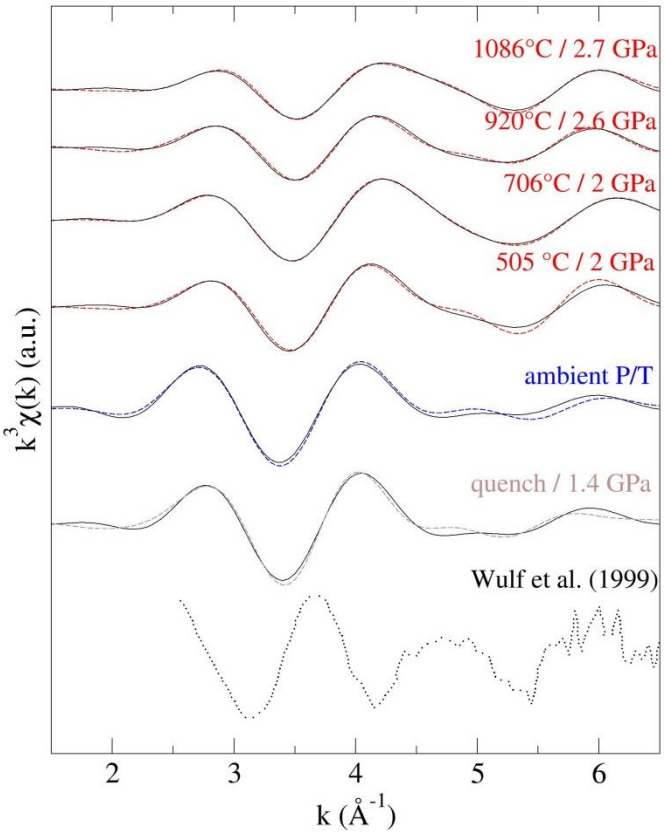

Figure 6: Shift of the Kr K-edge from 1.4 to 2.7 GPa (cf Table 2) compared to the standard reference value (14326 eV).